Possible Weyl-Luttinger phase transition in pyrochlore iridates revealed by Raman scattering

Predrag Nikolić [1,2,*] Yuanyuan Xu [2] Takumi Ohtsuki,[3] David C. Elbert,[4] Satoru Nakatsuji,[2,3,5,6,7] and Natalia Drichko[2]

[1]*Department of Physics and Astronomy, George Mason University, Fairfax, Virginia 22030, USA*
[2]*Institute for Quantum Matter and Department of Physics and Astronomy, Johns Hopkins University, Baltimore, Maryland 21218, USA*
[3]*Institute for Solid State Physics, University of Tokyo, Kashiwa, Chiba 277-8581, Japan*
[4]*Hopkins Extreme Materials Institute, Johns Hopkins University, Baltimore, Maryland 21218, USA*
[5]*Department of Physics, University of Tokyo, Bunkyo-ku, Tokyo 113-0033, Japan*
[6]*CREST, Japan Science and Technology Agency, Kawaguchi, Saitama 332-0012, Japan*
[7]*Trans-scale Quantum Science Institute, University of Tokyo, Bunkyo-ku, Tokyo 113-0033, Japan*

Pyrochlore iridates are thought to be a fertile ground for the realization of topologically nontrivial and strongly correlated states of matter. Here, we observe a magnetically driven phase transition between the topological Weyl semimetal and a Luttinger semimetal with quadratic band touching in $Nd_2Ir_2O_7$ using Raman scattering. We also find evidence of quadratic band touching in $Pr_2Ir_2O_7$, with the chemical potential further away from the node. Our theoretical analysis of the Raman scattering from Weyl and Luttinger quasiparticles agrees with experimental observations and enables a characterization of the material parameters while revealing interaction and disorder effects through a relatively short quasiparticle lifetime.

I. INTRODUCTION

Strongly correlated electrons with topologically nontrivial dynamics are among the most interesting physical systems that host unconventional states of matter [1–6]. The extreme topological interaction effect, electron fractionalization [7–9], is sought for quantum computing applications [10], while the more ubiquitous ability of interactions to shape phase transitions [11] is a means to obtain additional transport properties and control materials in devices [6]. Recent extensive studies have uncovered prominent realizations of magnetic Weyl semimetals that attract much attention in a vast range of fields, from basic science to applications [6,12–17]. Among topological magnets, pyrochlore iridates are a promising material family expected to host Weyl [18–22] and Luttinger semimetal states [23,24] as well as correlated topological insulator states [25,26]. Theoretically, these states universally emerge from a non-Fermi liquid quantum critical point [3,23,27–36] with quadratic band touching, which was predicted long ago [37].

The experimental exploration of the topological correlation physics in pyrochlore iridates is gaining momentum, but the confirmation and characterization of topologically nontrivial electron bands is still a challenge [18,23,24,26,38,39]. In $Nd_2Ir_2O_7$, where the higher-temperature paramagnetic phase is expected to host quadratic band touching, Weyl electrons would arise below $T_N = 33$ K due to the time-reversal symmetry (TRS) breaking associated with the antiferromagnetic order of Ir moments. This magnetic semimetal would persist down to $T = 14$ K when the system enters a fully

gapped semiconducting phase due to the ordering of Nd moments [26,39–41]. However, evidence for Weyl fermions could not be obtained with angle-resolved photoemission spectroscopy (ARPES) due to the low-energy resolution [38] and has been indicated with optical spectroscopy (although possessing unconventional properties caused by interactions) [39]. In this paper, we report the electronic contribution to Raman scattering in $Nd_2Ir_2O_7$ and $Pr_2Ir_2O_7$ and calculate the Raman response of Weyl and Luttinger nodal electrons using perturbation theory. By matching the measured frequency dependence of the Raman intensity with theory, we reveal the presence of Weyl quasiparticles in the low-temperature phase of the nearly stoichiometric $Nd_2Ir_2O_7$ as well as Luttinger quasiparticles in $Pr_2Ir_2O_7$ and the high-temperature phase of $Nd_2Ir_2O_7$. The magnetic ordering in $Nd_2Ir_2O_7$ at $T_N = 33$ K was detected by our Raman scattering experiment through the observation of magnons and will be discussed elsewhere [42]. In this paper, we finally reveal that this is also a topological phase transition associated with the splitting of the Luttinger quadratic band-touching node into a set of Weyl points, driven by the TRS breaking. The theory-experiment comparison allows us to also estimate the Fermi energy, quasiparticle lifetime, and other properties of the Weyl spectrum in $Nd_2Ir_2O_7$.

II. THEORY OF THE ELECTRONIC RAMAN SPECTRUM IN NODAL SEMIMETALS

Electrons contribute

$$\frac{\partial^2 \sigma}{\partial \Omega \partial \omega_s} = \frac{\omega_s}{\omega_i} \left(\frac{e^2}{mc^2} \right)^2 \chi''(\Omega) \tag{1}$$

*Contact author: pnikolic@gmu.edu

to the Raman differential scattering cross-section via two-photon processes in which a virtual particle-hole excitation is created by absorbing an incoming photon of frequency ω_i and quickly dissolved by emitting a scattered photon of frequency ω_s. The measured dependence of $\chi''(\Omega)$ on the energy transfer $\Omega = \omega_i - \omega_s$ to the electron gas (in units of $\hbar = 1$), known as *Raman shift frequency*, is an incoherent continuum without well-defined peaks because the transferred energy is shared by two free particles (electron and hole). Nevertheless, it provides rich information about the electron dynamics. If the quasiparticles with conduction and valence bands have an infinite lifetime, then $\chi''(\Omega)$ directly reflects the electronic density of states above a threshold frequency set by the chemical potential μ. The Raman amplitude $\chi''(\Omega) = -\frac{1}{\pi}\mathrm{Im}\{\chi(\Omega, \mathbf{q} \to 0)\}$ is extracted from a response function

$$\chi(\mathbf{q}, \Omega) = -i \sum_{\mathbf{k}\omega} \mathrm{tr}\{G(\mathbf{k}, \omega)\gamma_{\mathbf{k+q}}G(\mathbf{k+q}, \omega + \Omega)\gamma_{\mathbf{k}}\}, \quad (2)$$

where $G(\mathbf{k}, \omega)$ is the electron Green's function and $\gamma_{\mathbf{k}}$ is the Raman vertex function [43]. To capture the Weyl spectrum and basic interaction effects, we adopt a simple model Green's function:

$$G(\mathbf{k}, \omega) = \frac{A(\mathbf{k}, \omega)}{\omega - \left(\frac{k^2}{2m} + v\boldsymbol{\sigma}\mathbf{k} - \mu\right) + i\Gamma(\omega)\mathrm{sign}(\omega)}. \quad (3)$$

A quadratic term involving an effective mass m is retained to utilize the existing nonrelativistic theory of Raman scattering [43] while producing a more realistic spectrum. The pure relativistic limit is achieved simply by setting $m \to \infty$. The spin-orbit coupling involves the vector $\boldsymbol{\sigma}$ of Pauli matrices and gives the Green's function a matrix character. Since the Weyl Hamiltonian can be effectively expressed as a Hamiltonian $(\mathbf{k} - \mathcal{A})^2/2m$ of ordinary electrons coupled to an SU(2) gauge field $\mathcal{A} = -mv\boldsymbol{\sigma}$, the spin-orbit coupling is incorporated into the nonrelativistic Raman vertex merely by a momentum shift $\mathbf{k} \to \mathbf{k} - \mathcal{A}$. A finite quasiparticle lifetime τ is captured by the imaginary part $\Gamma(\omega) \propto \tau^{-1}$ of the electron self-energy correction. Coulomb interactions do not substantially alter the linear Weyl spectrum, so the electron dispersion assumed in the Green's function readily includes renormalizations inherited from the real part of the self-energy.

In case the chemical potential μ is shifted away from the exact position at the Weyl node, both intraband and interband transitions forming particle-hole pairs contribute to the electronic Raman amplitude $\chi''(\Omega)$. The former contributes [43]

$$\chi''(\Omega) \propto \frac{\tau\Omega}{1 + (\tau\Omega)^2} \quad (4)$$

and vanishes, as in ordinary metals when the quasiparticle lifetime τ is infinite. The interband part, calculated in Appendix A, is shown in Fig. 1(a) for the Weyl nodes whose spectrum has spherical symmetry. The essential structure of the Raman response is best appreciated in the idealized case of noninteracting Weyl electrons which have infinite lifetime, shown by the red discontinuous curve:

$$\chi''(\Omega) = \frac{m^2v\Omega^2}{2(2\pi)^3} \theta\left(\frac{|\Omega|}{2} - \left|\mu - \frac{\Omega^2}{8mv^2}\right|\right) I(\hat{\mathbf{e}}_s, \hat{\mathbf{e}}_i). \quad (5)$$
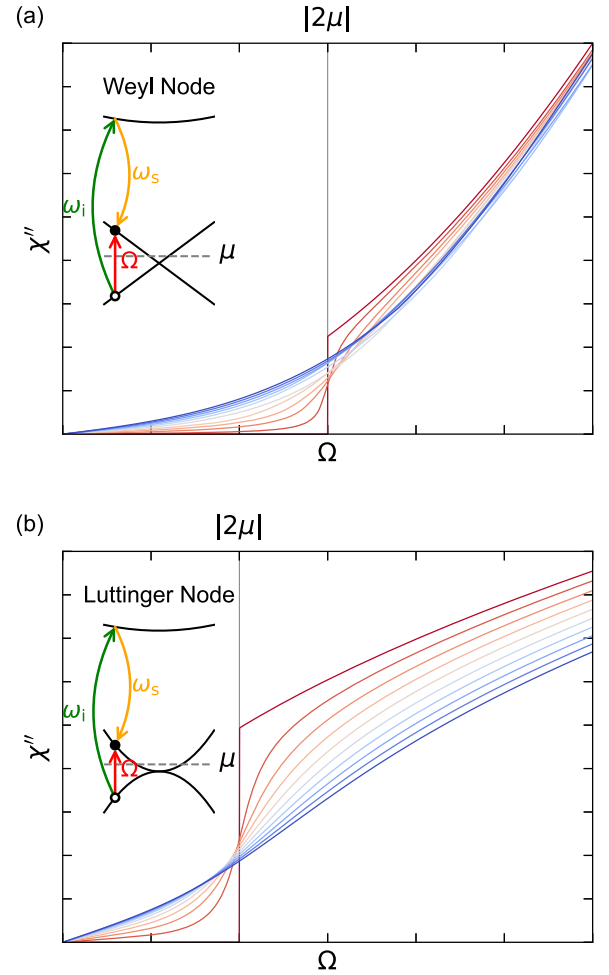

FIG. 1. Calculated frequency dependence of the Raman intensity from interband transitions of (a) Weyl and (b) Luttinger nodal quasiparticles. The vertical line indicates a threshold frequency $\Omega = |2\mu|$, below which the Raman scattering vanishes when the quasiparticles have infinite lifetime. The outermost red curve represents the infinite lifetime: It sharply drops to zero at $\Omega < |2\mu|$ and otherwise follows $\chi''(\Omega) \propto \Omega^2$ in (a) and $\chi''(\Omega) \propto \sqrt{\Omega}$ in (b). The other smooth curves are obtained with the inverse lifetime $\Gamma \propto \tau^{-1}$ increasing in steps of 0.1, up to 0.9 (expressed in the same arbitrary units as Ω).

In the relativistic limit $m \to \infty$ (well defined only for the measured differential scattering cross-section), the response occurs only above the Pauli threshold frequency $\Omega > |2\mu|$ for the generation of particle-hole excitations, where the chemical potential μ is expressed relative to the node energy. Above the threshold, the response follows the density of states $\chi''(\Omega) \propto \Omega^2$ of Weyl electrons. Realistically, however, interactions and disorder impart a finite lifetime on Weyl quasiparticles without qualitatively affecting the energy spectrum. A finite lifetime is seen to quickly fill in the Raman response below the threshold with a linear-looking frequency dependence. The analogous calculation of the Raman response in an idealized Luttinger semimetal [28], whose quasiparticles exhibit a quadratic band touching, produces $\chi''(\Omega) \propto \sqrt{\Omega}$ above the threshold $\Omega > |2\mu|$ which is characteristic for the density of states from a quadratic energy dispersion. The effect of

a finite Luttinger quasiparticle lifetime on interband Raman transitions is calculated in Appendix A and shown in Fig. 1(b).

III. ELECTRONIC RAMAN SPECTRUM MEASURED IN $Nd_2Ir_2O_7$ AND $Pr_2Ir_2O_7$

We compare our theoretical results on the Raman scattering response of the Luttinger and Weyl nodes to the experimental electronic Raman scattering spectra of $Nd_2Ir_2O_7$ and $Pr_2Ir_2O_7$. Earlier studies have suggested that the cubic symmetry should protect the existence of Luttinger nodal electrons with quadratic band touching in the paramagnetic state [28,37]. Applied to these particular pyrochlore iridates, both numerous band structure calculations [25,44–48] and some experimental results [23,24,38] point to the Luttinger node in the band structure of a paramagnetic state. Here, $Nd_2Ir_2O_7$ exhibits a phase transition associated with the magnetic ordering of the Ir moments at $T_N = 33$ K [39,42]. The broken TRS in the low-temperature phase with the ordered Ir moments is expected to split the Luttinger node into a set of Weyl nodes [19]. We observe evidence of this topological phase transition with Raman scattering.

The $Nd_2Ir_2O_7$ and $Pr_2Ir_2O_7$ Raman scattering spectra above 30 meV consist of sharp phonon modes [49] and magnon bands for $Nd_2Ir_2O_7$ in the low-temperature state, superimposed on a weaker broad electronic continuum; details are given in Appendix B and Ref. [42]. Raman response $\chi''(\Omega)$ in the (x, y) scattering channel contains E_g and T_{2g} components of scattering. We obtained the electronic contribution to the Raman scattering spectra by subtracting the phonon and magnon contributions from the Raman signal (see Appendix B for the detailed temperature dependence of the spectra and data analysis). The upper panel of Fig. 2 compares the experimental electronic Raman scattering spectrum of $Nd_2Ir_2O_7$ in the high-temperature paramagnetic ($T \sim$ 35–45 K) and low-temperature magnetic ($T \sim$ 20–30 K) phases. We observe a considerable difference between the frequency dependence of the electronic Raman continuum above and below the phase transition temperature, which can be well understood using our theoretical insight into the $\chi''(\Omega)$ response for Luttinger and Weyl nodes.

The Raman scattering of nodal electrons is dominated by interband transitions when the Fermi energy μ is close to the node energy. Such interband processes produce the Raman amplitude shown in Fig. 1. Alternatively, when the Fermi energy is shifted considerably from the band-touching energy, the ample charge carriers available in the ground state may dominate the Raman response at low frequencies and give rise to a conventional Raman signal [Eq. (4)] found in ordinary metals [43] and superconductors [50]. The two types of Raman response are qualitatively different, so a comparison of the measured electronic Raman response to the theoretical predictions can give us insight into the origin of the electronic scattering.

We compare the electronic Raman scattering spectra of $Nd_2Ir_2O_7$ to the theoretical models in Fig. 2(a). The paramagnetic phase in the temperature range $T \sim$ 30–45 K exhibits a Raman spectrum which can be naively fitted by two models: intraband transitions [Eq. (4)] of conventional charge carriers (CCC, black line), and interband transitions of Luttinger nodal
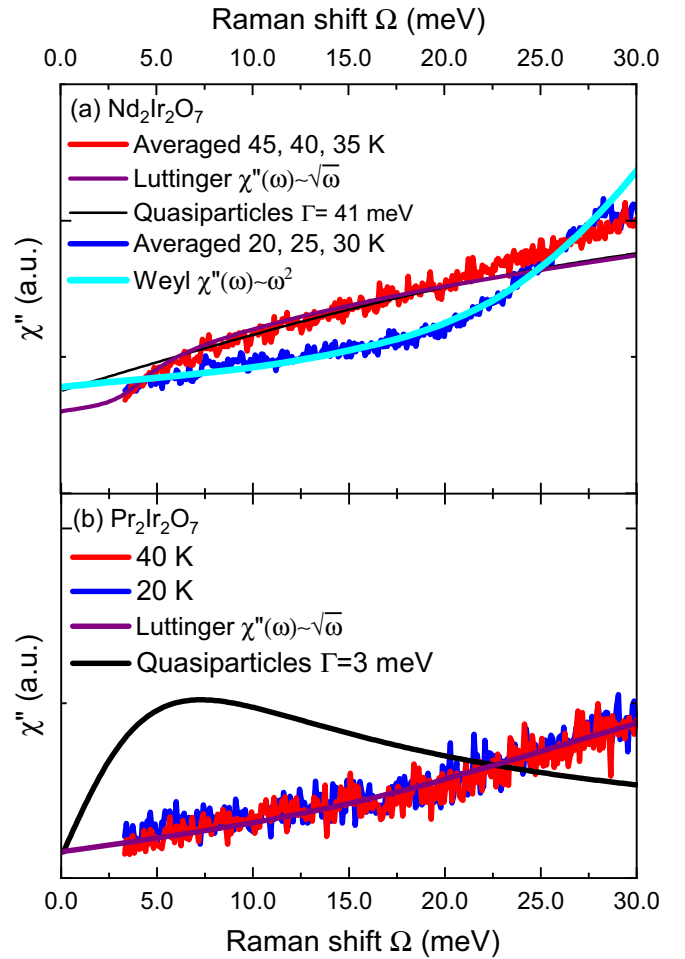

FIG. 2. Upper panel: Raman scattering spectra of $Nd_2Ir_2O_7$ (sample #1, 2% off-stoichiometry of Nd/Ir) above (red) and below (blue) the ordering temperature $T_N = 33$ K of Ir moments. The high-temperature spectrum is compared with the behavior of finite-lifetime charge carriers (black line) and interband transitions in the case of quadratic band touching (purple line; $\Gamma = 1.5$ meV, $|\mu| = 3$ meV). The low-temperature Raman spectrum is well described only by interband transitions of a Weyl semimetal (cyan line). Assuming that all Weyl nodes contributing to the Raman signal have the same node energy, we estimate the chemical potential $|\mu| \approx 10$ meV relative to the node ($\Gamma = 2.7$ meV). The evolution of the Raman spectrum from the quadratic to the Weyl nodelike appears to be abrupt within our temperature resolution. This can be explained by the negligible momentum transfers from photons to electrons, see Appendix A. Lower panel: Raman scattering spectra of $Pr_2Ir_2O_7$ in the temperature ranges 35–45 K (red) and 20–30 K (blue). These spectra are compared with the behavior of finite-lifetime charge carriers using the Γ values from Ref. [12] (black line) and interband transitions in the case of quadratic band touching where disorder and interactions give a linear-looking frequency dependence (purple line; $\Gamma = 5.8$ meV, $|\mu| = 11.7$ meV). Note that the interband transition fits in both panels do not include small charge carrier (Fermi surface) contributions in Eq. (4), but these contributions are visible in the low-frequency data as small deviations from the fits.

quasiparticles (LNQ, purple line). However, the LNQ model provides a better fit in a wider frequency range, and CCC fails in several ways. If the CCC fit is optimized at lowest
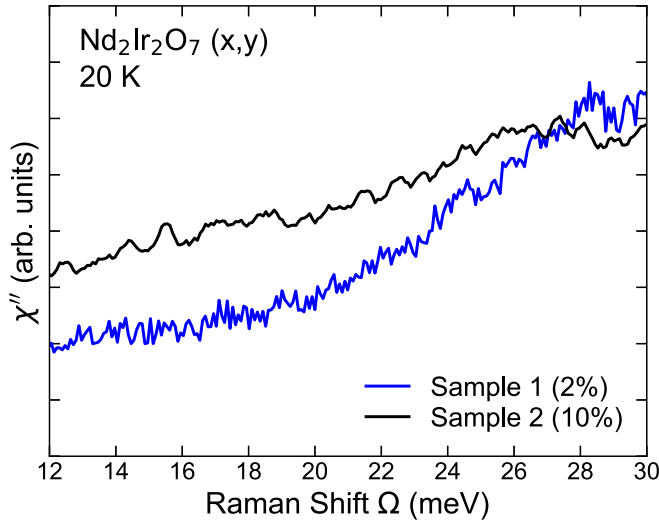
FIG. 3. Raman scattering spectra of two samples of $Nd_2Ir_2O_7$ with different amounts of disorder at $T = 20$ K, which is below T_N. Note the increase of Raman intensity compared with the response of sample #1 presented in Fig. 2 and the linear dependence on frequency for the samples with disorder. Structural disorder was characterized by resistivity measurements and phonon widths, see Appendix B for details.

frequencies, then the CCC curve eventually turns down and decreases away from the data with growing frequency. Otherwise, maximizing the frequency range in which the CCC curve fits well, as we have done, spoils its lowest-frequency behavior while requiring an unphysical relaxation rate $\Gamma \propto \tau^{-1} = 41$ meV of free charge carriers at $T \sim 35$–45 K [51]. The terahertz measurements performed on the related $Pr_2Ir_2O_7$ compound are consistent with considerably smaller Drude peak values, $\Gamma \approx 8.5$ meV in the $T \sim 30$–50 K range [24], like the values for $Nd_2Ir_2O_7$ [39].

A striking indication of nodal interband transitions is found in the magnetic phase at $T < T_N$. The Raman amplitude drops abruptly at $T < T_N$ across a wide frequency range but picks up and grows at higher frequencies. The drop is abrupt due to the negligible momentum transfers from photons to electrons, as explained in Appendix A. In this temperature range, the Raman spectrum is described best by the interband transitions of Weyl electrons with a finite lifetime. In Fig. 2(a), we compare the experimental spectra to the theoretical curve of $\chi''(\Omega)$ for Weyl nodes with $\Gamma = 2.7$ meV and $|\mu| = 10$ meV, which produces good agreement up to about $\Omega \sim 30$ meV which could be the energy cutoff for the linear Weyl spectrum. The quantity $\chi''(\Omega)$ is not very sensitive to small changes of parameters, so $|\mu| = 10$ meV in the magnetic phase was selected to be close to the cutoff associated with the charge carrier contribution to the infrared (IR) spectra of $Nd_2Ir_2O_7$ at these temperatures [39].

Figure 3 compares the $T = 20$ K electronic Raman scattering spectra of two different samples of $Nd_2Ir_2O_7$, one with minimum disorder, as presented in Fig. 2(a), and another with structural disorder due to deviation of Nd/Ir stoichiometry by $\sim 10\%$. Appendix B presents the Raman characterization of structural disorder. Disorder reduces the lifetime of excitations and hence changes the frequency dependence of the

electronic response (see Fig. 1). We observe a change of the electronic scattering with increasing disorder, where the low-frequency contribution to $\chi''(\Omega)$ becomes linear and increases in intensity, masking the $\chi''(\Omega) \propto \Omega^2$ behavior, as predicted by the calculations.

An example of a quadratic node which is preserved on cooling between 40 and 20 K is provided by $Pr_2Ir_2O_7$. The electronic band structure of this material is like that in the paramagnetic state of $Nd_2Ir_2O_7$ but with μ shifted further away from the nodal position. Studies of $Pr_2Ir_2O_7$ films suggest a shift up to 17 meV [24]. There is evidence of $Pr_2Ir_2O_7$ crystals showing disordered electronic potential [52]. In Fig. 2(b), we present experimental electronic Raman scattering data for $Pr_2Ir_2O_7$, which show the same response for 40 and 20 K, in accordance with the absence of changes of magnetic or electronic structure in this temperature range. A comparison with the conventional response of charge carriers [Eq. (4)], using $\Gamma = 3$ meV at 20 K from the terahertz spectroscopy studies [24] (black curve), shows that the electronic Raman response is determined by the transitions within the quadratic node. The linear dependence of the experimental $\chi''(\Omega)$ up to ~ 25 meV in the spectra of $Pr_2Ir_2O_7$ corresponds to the situation with a high chemical potential ($|\mu| > 11$ meV) and low lifetime of excitations due to the disorder expected for this material. We have to note here that the decrease of the quasiparticle lifetime, which leads to the linear frequency dependence of the Raman scattering continuum, reduces the distinctions between the responses of the Luttinger and Weyl nodes.

IV. DISCUSSION

In conclusion, the electronic Raman scattering of $Nd_2Ir_2O_7$ agrees well with the calculation of Raman response by interband excitations. The incoherent $\chi'' \sim \Omega^2$ response from Weyl nodes at $T < T_N$ and $\chi'' \sim \sqrt{\Omega}$ response from Luttinger nodes at $T > T_N$ are not easy to obtain by alternative mechanisms. Specifically, the interband response of Weyl electrons cannot be confused with intraband transitions across a Fermi surface. Instead, some contamination of the response could come from the transitions involving higher-energy states within the Weyl spectrum where the electron dispersion becomes nonlinear. Generally, a lattice Weyl-electron model will produce a nonlinear low-energy spectrum $E_{\mathbf{k}} \sim vk + \alpha k^l$. The subdominant power $l > 1$, treated using the effective mass approximation [43], gives $\chi''(\Omega) \sim |\Omega|^{2(l-1)+d-3}$ beyond the threshold ($d = 3$ describes the Weyl materials and $d = 2$ describes graphene). The $l = 2$ power, contributing to $\chi'' \sim \Omega^2$, was considered here through the mass parameter m (without relying on the effective mass approximation). Other powers $l \geqslant 3$ produce qualitatively different Raman spectra which are not seen in the experiment. Note that virtual transitions to higher-energy bands cannot contaminate the Raman response of Weyl electrons because the effective mass approximation, well justified in this case, predicts a vanishing Raman vertex $\gamma_{\mathbf{k}}$, and hence, $\chi'' = 0$, for the linear energy spectrum.

The interband and intraband responses of electrons with quadratic band touching are notably harder to distinguish, but in $Nd_2Ir_2O_7$, we presented two arguments in favor of the interband transitions. Another argument can be based on

the observation in Fig. 2 that the electronic density of states clearly migrates to lower energies upon the transition to the paramagnetic phase. This must drag the chemical potential μ toward the node energy. Since μ was already close to the node energy in the magnetic Weyl-node phase, it can only get closer to the node in the Luttinger-node phase and hence promote the interband Raman transitions. The migration of μ to a lower energy contributes to the fact that no apparent threshold frequency is seen in the Raman spectrum of the paramagnetic phase.

The changes of electronic Raman spectrum can sometimes be attributed to a pseudogap. This is very unlikely to be relevant for the materials we studied. Pseudogap is associated with strong electron correlations which partially gap out the Fermi surface. Our data are consistent with the response of nodal electrons across an extended energy range, instead of quasiparticles near a Fermi surface. Furthermore, the characteristic drop in the density of states seen in $Nd_2Ir_2O_7$ occurs at the magnetic phase transition temperature. The magnetic moments, evidently responsible for the electronic spectrum change, are large and have mostly classical dynamics. This is not conducive to pseudogap physics. Similarly, we see no evidence of localization or pairing in charge dynamics (see Appendix B), which might be associated with a pseudogap.

A Raman experiment alone can reliably distinguish between the true nodal spectrum and the presence of a small band gap only if electrons have a long lifetime and the Fermi energy sits exactly at the putative node energy. Otherwise, the judgment in favor of nodes must rely on theoretical node protection mechanisms: topological in the case of a linear Weyl spectrum [19] and cubic symmetry-based in the case of a Luttinger quadratic band touching [37]. Raman scattering can be a useful tool for identifying the electronic structure in other Luttinger semimetals (e.g., BC-8 Si [53]), Weyl semimetals (e.g., VNb_3S_6 [54]), and Dirac systems [55–58].

The quadratic nodal spectrum is additionally important as a non-Fermi liquid quantum critical point strongly affected by Coulomb interactions [24,27–29]. It has been predicted [59] that the Raman response $\chi'' \sim |\Omega|^{(1/2)+\delta}$ in this state acquires a small correction $\delta \approx \frac{9}{76}$. This is difficult to experimentally discern without a pristinely accurate fit at low energies. Further studies are needed to determine if the Fermi energy in quadratic band-touching scenarios indeed sits close enough to the nodes [23,45] to activate the non-Fermi liquid physics. Looking toward the future, it is highly important to reveal the characters of the non-Fermi liquid excitations by tuning the Fermi level to the node.

V. CONCLUSIONS

We developed a theory of electronic Raman scattering in Weyl and Luttinger semimetals and measured the electronic contribution to Raman scattering in $Nd_2Ir_2O_7$ and $Pr_2Ir_2O_7$. The experiment reveals a topological phase transition from a quadratic band-touching spectrum (Luttinger semimetal) to a Weyl electronic spectrum at the onset of magnetic order in $Nd_2Ir_2O_7$. No such transition is observed in $Pr_2Ir_2O_7$, but its spectrum is consistent with quadratic band touching in the entire measured temperature range. Our results show that Raman scattering can be used as a reliable probe of the electron band topology in correlated materials.

APPENDIX A: ELECTRONIC RAMAN SCATTERING CROSS-SECTION FROM INTERBAND TRANSITIONS

The matrix elements of the electronic Raman vertex function $\gamma_{\mathbf{k}}$ in Eq. (2) are given by [43]

$$\gamma_{\alpha\beta}^{i,s} = \langle \alpha | \gamma_{\mathbf{k}} | \beta \rangle = \hat{\mathbf{e}}_i \hat{\mathbf{e}}_s \rho_{\alpha\beta}(\mathbf{q}_i - \mathbf{q}_s) + \frac{1}{m}\sum_{\gamma}$$

$$\times \left[\frac{p_{\alpha\gamma}(\hat{\mathbf{e}}_s, -\mathbf{q}_s)p_{\gamma\beta}(\hat{\mathbf{e}}_i, \mathbf{q}_i)}{E_\beta - E_\gamma + \omega_i} \right. $$
$$\left. + \frac{p_{\alpha\gamma}(\hat{\mathbf{e}}_i, \mathbf{q}_i)p_{\gamma\beta}(\hat{\mathbf{e}}_s, -\mathbf{q}_s)}{E_\beta - E_\gamma - \omega_s} \right], \tag{A1}$$

where

$$\rho_{\alpha\beta}(\mathbf{q}) = \rho_{\beta\alpha}^*(-\mathbf{q}) = \langle \alpha | e^{i\mathbf{q}\mathbf{r}} | \beta \rangle,$$

$$p_{\alpha\beta}(\hat{\mathbf{e}}, \mathbf{q}) = p_{\beta\alpha}^*(\hat{\mathbf{e}}, -\mathbf{q}) = \hat{\mathbf{e}} \langle \alpha | e^{i\mathbf{q}\mathbf{r}}(-i\nabla - \sigma^a \mathbf{A}^a) | \beta \rangle. \tag{A2}$$

The initial $|\beta\rangle$ and final $|\alpha\rangle$ states of the quasiparticle have momenta $\mathbf{k}$ and $\mathbf{k} + \mathbf{q}$, respectively, with $\mathbf{q}$ being the momentum transfer from the photon to the electrons. The polarizations of the incoming (i) and scattered (s) photon are given by $\hat{\mathbf{e}}_i$ and $\hat{\mathbf{e}}_s$, respectively. The SU(2) gauge field $\mathcal{A} = \mathbf{A}^a \sigma^a = -mv\boldsymbol{\sigma}$ embodies the spin-orbit coupling which produces the Weyl spectrum, as explained in Sec. II.

The electron Green's function shaped by disorder and interactions is modeled as

$$G(\mathbf{k}, \omega) = \frac{A(\mathbf{k}, \omega)}{\omega - H_{\mathbf{k}} + i\Gamma(\mathbf{k}, \omega)\,\text{sign}(\omega)}. \tag{A3}$$

For simplicity, we ignore the spin, frequency, and momentum dependence of the spectral weight $A_\sigma(\mathbf{k}, \omega) \approx 1$ and the imaginary self-energy part $\Gamma(\mathbf{k}, \omega) \approx \Gamma > 0$. Despite being very crude, this approximation faithfully retains the essential effects of all processes which impart a finite lifetime $\tau \propto \Gamma^{-1}$ on the electronic quasiparticles. The matrix representation $H_{\mathbf{k}}$ of the single-particle Hamiltonian depends on the type of the nodal spectrum.

1. Weyl spectrum

The spherically symmetric Weyl spectrum is obtained from $H_{\mathbf{k}} = k^2/2m + v\boldsymbol{\sigma}\mathbf{k}$. The mass parameter $m \neq 0$ allows us to both apply the existing nonrelativistic theory of Raman scattering and extract the relativistic behavior by taking the $m \to \infty$ limit at the end. In the representation which diagona-

lizes $H_{\mathbf{k}}$, the interband electron scattering contributes

$$\chi(\mathbf{q} \to 0, \Omega) = -i \int \frac{d^3 k}{(2\pi)^3} \sum_\sigma \gamma_{\sigma,-\sigma}^{\mathrm{i,s}}(\mathbf{k}) \, \gamma_{-\sigma,\sigma}^{\mathrm{s,i}}(\mathbf{k}) \, I_\sigma(\Omega)$$

to the Raman response function, where

$$I_\sigma(\Omega) = \int \frac{d\omega}{2\pi} \frac{1}{\omega - \frac{\Omega}{2} - E_{\mathbf{k},-\sigma} + i\Gamma \mathrm{sign}\!\left(\omega - \frac{\Omega}{2}\right)} \frac{1}{\omega + \frac{\Omega}{2} - E_{\mathbf{k},\sigma} + i\Gamma \mathrm{sign}\!\left(\omega + \frac{\Omega}{2}\right)}, \tag{A4}$$

$\sigma = \pm 1$ and $E_{\mathbf{k}\sigma} = k^2/2m + \sigma v k$. This frequency integral can be calculated directly. The imaginary part of χ yields the interband contribution to the Raman scattering rate:

$$\chi''(\Omega) = \frac{1}{\pi} \int \frac{d^3 k}{(2\pi)^3} \sum_\sigma \gamma_{\sigma,-\sigma}^{\mathrm{i,s}}(\mathbf{k}) \, \gamma_{-\sigma,\sigma}^{\mathrm{s,i}}(\mathbf{k}) \, \mathrm{Re}\{I_\sigma(\Omega)\} = \frac{(mv^2)^2}{2\pi^4} I(\hat{\mathbf{e}}_{\mathrm{s}}, \hat{\mathbf{e}}_{\mathrm{i}}) \int_0^\infty dk \, k^2 \sum_\sigma \mathrm{Re}\{I_\sigma(|\Omega|)\}, \tag{A5}$$

with

$$2\pi \, \mathrm{Re}\{I_\sigma(|\Omega|)\} = \frac{1}{2}\left[\frac{|\Omega| - 2\sigma v k}{(|\Omega| - 2\sigma v k)^2 + 4\Gamma^2} - \frac{1}{|\Omega| - 2\sigma v k} \right]\left\{ \ln\left[\frac{E_{\mathbf{k},\sigma}^2 + \Gamma^2}{(E_{\mathbf{k},-\sigma} + |\Omega|)^2 + \Gamma^2} \right] + \ln\left[\frac{E_{\mathbf{k},-\sigma}^2 + \Gamma^2}{(E_{\mathbf{k},\sigma} - |\Omega|)^2 + \Gamma^2} \right] \right\}$$

$$+ \frac{2\Gamma}{(|\Omega| - 2\sigma v k)^2 + 4\Gamma^2}\left[\arctan\left(\frac{E_{\mathbf{k},-\sigma} + |\Omega|}{\Gamma} \right) - \arctan\left(\frac{E_{\mathbf{k},\sigma} - |\Omega|}{\Gamma} \right) + \arctan\left(\frac{E_{\mathbf{k},\sigma}}{\Gamma} \right) \right.$$

$$\left. - \arctan\left(\frac{E_{\mathbf{k},-\sigma}}{\Gamma} \right) \right]. \tag{A6}$$

The Raman vertex in Eq, (A1) for Weyl electrons is dominated by the intermediate states γ which belong to the nodal spectrum just like the initial β and final α states. The intermediate states from higher bands can be handled by the effective mass approximation [43], but their effect is negligible (formally vanishes) due to the linear relativistic character of the low-energy Weyl spectrum. Focusing on the nodal states only, it will suffice for our purposes to argue that the Raman vertex is approximately independent of the momentum magnitude $|\mathbf{k}|$. First, as usual in condensed matter systems, we may neglect the momentum transfer $\mathbf{q}$ from the photon to the electrons. Then all states α, β, γ live at the same momentum $\mathbf{k}$, and γ can coincide either with α or β. The diamagnetic term $\rho_{\alpha\beta}$ in Eq. (A1) vanishes for interband transitions ($\alpha \neq \beta$). In the other part of Eq. (A1), one denominator at $\gamma = \alpha$ is equal to the other at $\gamma = \beta$ and reduced either to just ω_{i} or ω_{s} due to energy conservation $\Omega = E_\alpha - E_\beta = \omega_{\mathrm{s}} - \omega_{\mathrm{i}}$. The corresponding numerators each pick the matrix elements of the gauged momentum operator as $p_{\uparrow\downarrow} \propto \langle\alpha|\mathcal{A}|\beta\rangle$ and $p_{\uparrow\uparrow}, p_{\downarrow\downarrow} \propto \mathbf{k} + \langle\alpha|\mathcal{A}|\beta\rangle$; the momentum dependence of the latter cancels out once the two fractions with equal denominators are added up.

The integrals over the direction and magnitude of $\mathbf{k}$ in Eq. (A5) are separable because I_σ depends only on $|\mathbf{k}|$, and the Raman vertex $\gamma_{\mathbf{k}}$ depends (approximately) only on $\hat{\mathbf{k}}$. Then the polarization dependence is fully contained in the factor $I(\hat{\mathbf{e}}_{\mathrm{s}}, \hat{\mathbf{e}}_{\mathrm{i}})$ constructed from the $\hat{\mathbf{k}}$ integral. This factor is not important for our present purpose. The dependence of the Raman scattering rate on the shift frequency Ω follows only from the remaining momentum-magnitude integral in Eq. (A5), which we calculate numerically and plot in Fig. 1(a).

2. Quadratic band-touching spectrum

A model Hamiltonian displaying quadratic band touching has been constructed in the context of pyrochlore iridates [28]:

$$H_{\mathbf{k}} = \frac{k^2}{2\widetilde{M}_0} + \frac{\frac{5}{4}k^2 - (\mathbf{k}\mathbf{J})^2}{2m'} - \frac{(k_x J_x)^2 + (k_y J_y)^2 + (k_z J_z)^2}{2M_{\mathrm{c}}}. \tag{A7}$$

It involves three mass parameters $\widetilde{M}_0, M_{\mathrm{c}}, m'$ and the $S = \frac{3}{2}$ matrix representations of spin-projection operators J_x, J_y, J_z. The twofold degenerate conduction $\sigma = 1$ and valence $\sigma = -1$ bands in the spectrum of this Hamiltonian touch quadratically at $\mathbf{k} = 0$ in a certain domain of mass parameters.

Since the spectrum is quadratic, we can apply the effective mass approximation [43] to calculate the Raman vertex function:

$$\gamma_{\mathbf{k}} \approx m \, \hat{e}_i^a \hat{e}_s^b \frac{\partial^2 H_{\mathbf{k}}}{\partial k^a \partial k^b}$$

$$= m \, \hat{e}_i^a \hat{e}_s^b \left(\frac{\delta_{ab}}{M_0} + \frac{\frac{5}{2}\delta_{ab} - \{J_a, J_b\}}{2m'} - \frac{J_a^2 \delta_{ab}}{M_c} \right). \tag{A8}$$

We can obtain the frequency dependence of the Raman scattering cross-section more easily by neglecting the momentum transfer $\mathbf{q}$ from the photon to the electrons. In this approximation, the matrix elements $\gamma_{\alpha\beta}^{\mathrm{i,s}}$ of the Raman vertex do not depend on the momentum magnitude $|\mathbf{k}|$. Interband transitions are considered by the expression for the scattering rate analogous to Eq. (A5):

$$\chi''(\Omega) = \frac{1}{\pi} \sum_{nn'} \int \frac{d^3 k}{(2\pi)^3} \sum_\sigma \gamma_{\sigma n,-\sigma n'}^{\mathrm{i,s}}(\mathbf{k}) \, \gamma_{-\sigma n',\sigma n}^{\mathrm{s,i}}(\mathbf{k})$$
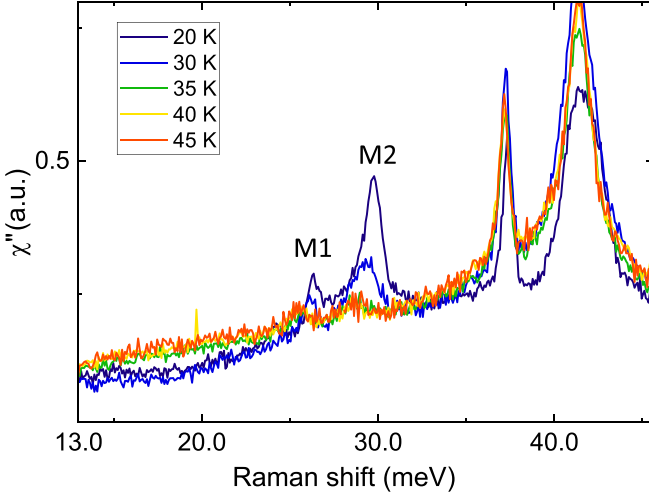
$$\times \mathrm{Re}\{I_\sigma(\mathbf{k}, \Omega)\}, \tag{A9}$$

FIG. 4. Raman scattering spectra of $Nd_2Ir_2O_7$ in the $\hat{z}(xy)z$ polarization. The labeled M1 and M2 peaks are magnon excitations which appear in the $Nd_2Ir_2O_7$ Raman spectrum below the critical temperature $T_N = 33$ K of magnetic ordering. Peaks at 38 and 41 meV belong to phonon excitations. Note the gradual increase of intensity of magnon peaks at T_N.

with the main new ingredients being a different spectrum and the summation over a larger set of quantum numbers involving a two-valued index n which distinguishes the degenerate bands. The function $Re\{I_\sigma\}$ obtained from the frequency integral is universally given by Eq. (A6) but with $2\sigma vk$ systematically replaced by the interband energy difference $E_{\mathbf{k},\sigma} - E_{\mathbf{k},-\sigma}$ appropriate for the Luttinger nodal spectrum. The cubic anisotropy complicates calculations without imparting any special qualitative features on Raman scattering. If the spectrum is approximated by an isotropic one, we can again separate the integrals over the direction and magnitude of $\mathbf{k}$. The direction integral is relevant only for the light-polarization dependence of the Raman response, and the momentum integral can be calculated in a straightforward manner numerically, as in the case of Weyl electrons. The resulting dependence of the Raman scattering on the shift frequency Ω is plotted in Fig. 1(b). The behavior $\chi''(\Omega) \propto \sqrt{|\Omega|}$ beyond a threshold frequency in the infinite lifetime limit ($\Gamma \to 0$) is physically determined by the electronic density of states.

3. Phase transition between quadratic and Weyl nodes

In $Nd_2Ir_2O_7$, iridium magnetic moments order at the critical temperature $T_N = 33$ K. This is a second-order phase transition judging by the thermodynamic and optical probes [39] as well as the gradual development of magnon peaks in the Raman spectrum below the critical temperature shown in Fig. 4. However, the electronic Raman scattering continuum, which displays a clear distinction between quadratic band touching and Weyl nodes in Fig. 2(a), evolves abruptly. An explanation of this unusual behavior is found in the negligible momentum transfers caused by photons.

In the paramagnetic phase, electronic bands are spin-degenerate and not Dirac-like, so the photons are not constrained by momentum conservation in the manner they
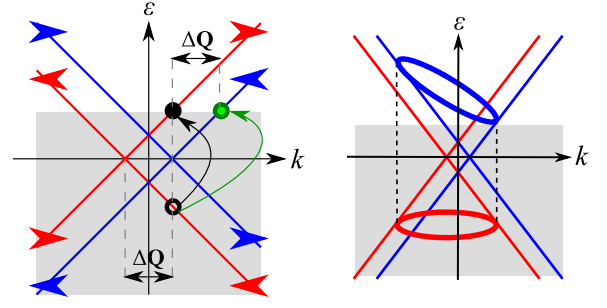

FIG. 5. (Left) Intranode spin-flip transitions of Weyl electrons occur with no momentum transfer above the threshold energy $2|\mu|$ imposed by the Fermi sea (shaded). In contrast, typical spin-preserving transitions would require momentum transfers $\Delta\mathbf{Q}$ equal to the Weyl-node momentum separation, which the photons cannot provide. Here, we assume that $|\Delta\mathbf{Q}|$ grows in proportion to the magnetization, as a power of $T_N - T$ below the magnetic transition in $Nd_2Ir_2O_7$. (Right) Alternatively, nearly spin-preserving internode transitions with zero momentum transfers may be permitted by energy and momentum conservation. However, such transitions are suppressed by the mechanism which conserves the chiral current of massless Dirac electrons. The suppression would be complete in the absence of the chiral quantum anomaly and, in that manner, strongest when $\Delta\mathbf{Q} \to 0$. On the other hand, the energy cutoff $\mathcal{E}_c$ of the realistic Weyl spectrum quickly suppresses all possible internode transitions with zero momentum transfer when $v|\Delta\mathbf{Q}| > \mathcal{E}_c$, where v is the Fermi velocity (slope of the Weyl spectrum). Therefore, the characteristic frequency dependence of the Raman continuum is dominated by the intranode transitions and can sharply distinguish the Weyl nodes from quadratic band touching.

couple to the electron spin. This changes at the $T = T_N$ onset of TRS breaking when the electronic spectrum acquires dipoles of Weyl nodes. Magnetization is small just across this second-order transition, so the opposite-chirality Weyl nodes are presumably close to each other in momentum space. However, the separation between the Weyl nodes is measured in momentum units; a small separation for electrons is large for photons. If the speed of light were comparable with the Fermi velocity, one would see a gradual evolution of the electronic continuum in the Raman spectrum. Instead, the selection rules for photon absorption/emission with negligible momentum transfers (on the electronic scales) prohibit electron scattering from one Weyl node to another. This is illustrated in Fig. 5. In other words, photons see well-formed Weyl nodes up to the cutoff energy scale almost immediately after the transition. Given that the Fermi velocity is at least two orders of magnitude smaller than the speed of light, observing a gradual evolution of the electronic Raman spectrum probably requires a quite high (millikelvin) temperature resolution.

APPENDIX B: EXPERIMENTAL METHODS

1. Raman scattering spectroscopy

Raman scattering spectra of $Nd_2Ir_2O_7$ and $Pr_2Ir_2O_7$ were collected using the Horiba Jobin-Yvon T64000 triple monochromator spectrometer with a liquid nitrogen cooled CCD detector. The 514.5 nm line of Ar^+-Kr^+ mixed gas laser was used as the excitation light. The measurements
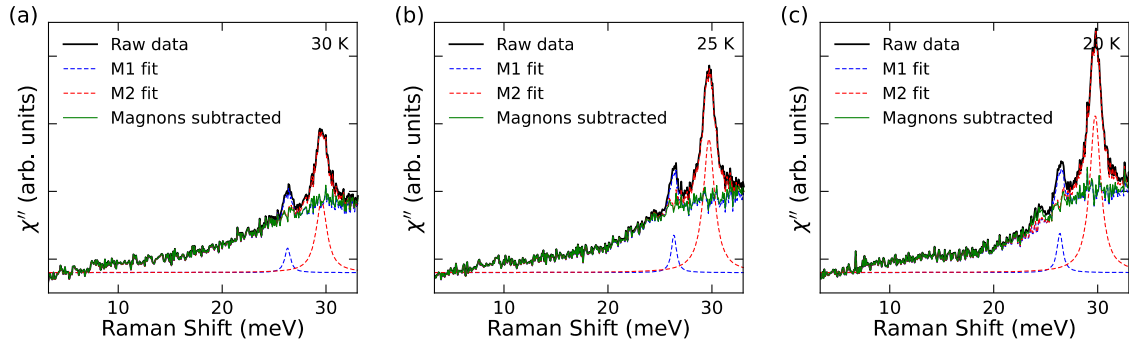
FIG. 6. Raw Raman scattering data of $Nd_2Ir_2O_7$ at temperatures below T_N, fits of magnon excitations and the resulting spectra of the electronic continuum, presented in Figs. 2 and 3.

were performed for single crystals of these materials, using as-grown octahedron-shaped (111) facets with size of ~ 1 mm in each dimension. Measurements were done in the pseudo-Brewster's angle geometry with a laser probe of 50 by 100 µm in size; the laser power used was varied between 3 and 15 mW, with the estimated heating of the sample of 1 K per 1 mW of laser power. For low-temperature measurements, the samples were mounted on the cold finger of a Janis ST-500 cryostat.

In the main text, we presented the data obtained with the $\hat{z}(xy)z$ polarization to separate the electronic Raman scattering in $Nd_2Ir_2O_7$ we are interested in from the A_{1g} magnetic scattering. Spectra including phonons in all polarizations for $Nd_2Ir_2O_7$ are presented in Ref. [42]. Raman phonon spectra of $Pr_2Ir_2O_7$ are presented in Ref. [49]. To correct for the small deviations ($< 20\%$ for the same excitation power) of the intensity of Raman response in different measurements, all the spectra were normalized to the intensity of the A_{1g} phonon. The intensity of all spectra was normalized by the thermal factor $[n(\omega, T) + 1]$, where $n(\omega, T)$ is the Bose occupation factor.

The electronic Raman continuum spectra presented in Figs. 2 and 3 were obtained by subtracting magnon features from the original spectra, which will be published elsewhere [42]. Specifically, the original spectra were fitted with several Lorentzian shapes, and those relevant to magnons were subtracted, as shown in Fig. 6. Note that all phonons appear in the spectra at frequencies above the electronic continuum of interest. In Fig. 4, we present original data obtained in the $\hat{z}(xy)z$ polarization. Note that the part of the spectra <35 meV, related to the electronic continuum, overlaps within the experimental noise level for temperatures in the ranges of 45–35 K and 30–20 K. This allowed us to average the data in that range to reduce the resulting noise in the spectra.

2. Information about the samples and their characterization

Single crystals of $Nd_2Ir_2O_7$ and $Pr_2Ir_2O_7$ were grown by KF flux methods described in detail in Ref. [60]. As discussed in Ref. [26], $Nd_2Ir_2O_7$ crystals produced by this method of synthesis can deviate from stoichiometry in the Nd/Ir ratio, which can be slightly >1. It was shown that this off-stoichiometry results in the decrease of the resistivity, and temperature dependence of resistivity is a sensitive tool to characterize $Nd_2Ir_2O_7$ crystals. A systematic study of the effects of the substitution of the Ir site was done
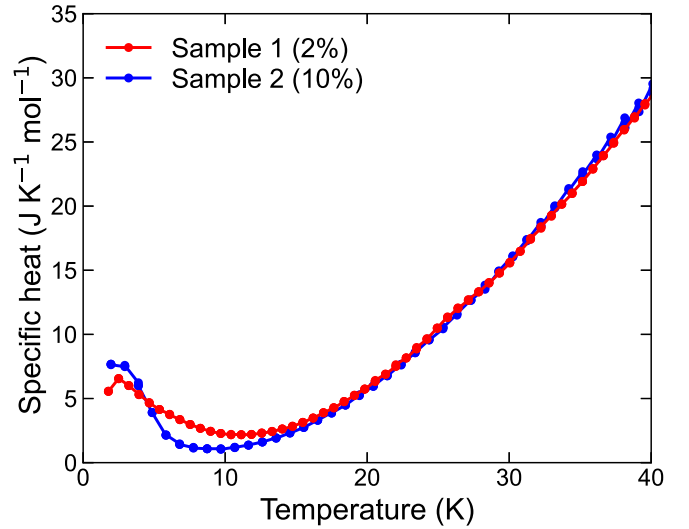

FIG. 7. Temperature dependence of the specific heat for the $Nd_2Ir_2O_7$ samples with different Nd/Ir stoichiometry: sample #1 (red curve) and sample #2 (blue curve).
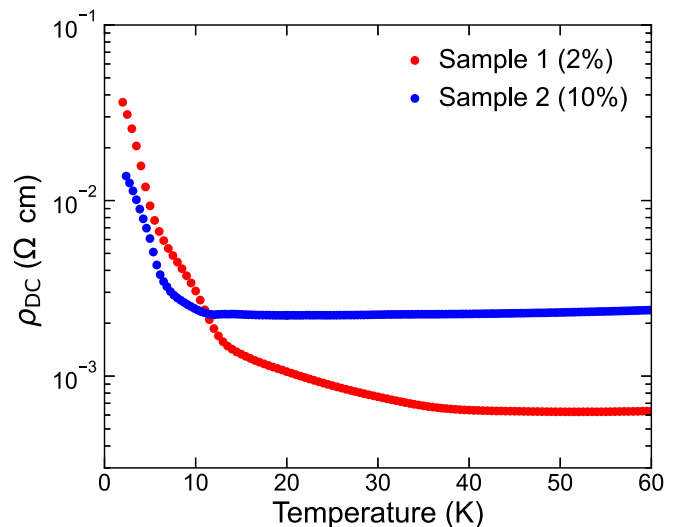

FIG. 8. Temperature dependence of the resistivity for the $Nd_2Ir_2O_7$ samples with different Nd/Ir stoichiometry: sample #1 (red curve) [39] and sample #2 (blue curve).

for the range of samples where Ir is substituted with Rh, $Nd_2(Ir_{1-x}Rh_x)_2O_7$ [61], resulting in similar effects on the heat capacity and resistivity.

Figure 3 presents the data for two different crystals of $Nd_2Ir_2O_7$ with different Nd/Ir off-stoichiometry which was determined as described below.

To directly probe the ratio of Nd/Ir by a nondestructive method, we used energy dispersive x-ray (EDX) spectrometry [62] with the Thermo Scientific Helios G4 UC FIBSEM setup. The results show that Nd/Ir has no more than 2% off-stoichiometry for sample #1, and 10% for sample #2. The precision of this method is limited to at least 2% due to systematic errors in determining the amount of Nd; however,

the relative amounts are determined with the precision of at least 1%. Since the precision of this method is limited, while the properties of the material were shown to be very sensitive to stoichiometry [61], we used heat capacity, resistivity, and phonon Raman scattering to characterize the samples.

The most stoichiometric sample of $Nd_2Ir_2O_7$ (sample #1) is the same crystal that was studied in Ref. [63] by means of IR/terahertz spectroscopy, resistivity, and heat capacity. Heat capacity data were reproduced in this paper and are presented in Fig. 7 together with the data for sample #2. Resistivities of these two samples are presented in Fig. 8. The suppression of the feature of the transition at 33 K we observe for the more disordered sample is in agreement with the tendencies observed in comparison with Ref. [61].

---

[1] N. Nagaosa and Y. Tokura, Topological properties and dynamics of magnetic skyrmions, Nat. Nanotechnol. **8**, 899 (2013).

[2] A. Fert, V. Cros, and J. Sampaio, Skyrmions on the track, Nat. Nanotechnol. **8**, 152 (2013).

[3] W. Witczak-Krempa, G. Chen, Y. B. Kim, and L. Balents, Correlated quantum phenomena in the strong spin-orbit regime, Annu. Rev. Condens. Matter Phys. **5**, 57 (2014).

[4] H. Takagi, T. Takayama, G. Jackeli, G. Khaliullin, and S. E. Nagler, Concept and realization of Kitaev quantum spin liquids, Nat. Rev. Phys. **1**, 264 (2019).

[5] C. Broholm, R. J. Cava, S. A. Kivelson, D. G. Nocera, M. R. Norman, and T. Senthil, Quantum spin liquids, Science **367**, eaay0668 (2020).

[6] S. Nakatsuji and R. Arita, Topological magnets: Functions based on Berry phase and multipoles, Annu. Rev. Condens. Matter Phys. **13**, 119 (2022).

[7] X.-G. Wen, *Quantum Field Theory of Many-Body Systems* (Oxford University Press, New York, 2004).

[8] T. Senthil and M. P. A. Fisher, Z_2 gauge theory of electron fractionalization in strongly correlated systems, Phys. Rev. B **62**, 7850 (2000).

[9] P. Nikolić, Topological orders of monopoles and hedgehogs: From electronic and magnetic spin-orbit coupling to quarks, Phys. Rev. B **101**, 115144 (2020).

[10] P. Bonderson, S. D. Sarma, M. Freedman, and C. Nayak, A blueprint for a topologically fault-tolerant quantum computer, arXiv:1003.2856.

[11] S. Sachdev, *Quantum Phase Transitions* (Cambridge University Press, Cambridge, 1999).

[12] N. P. Armitage, E. J. Mele, and A. Vishwanath, Weyl and Dirac semimetals in three-dimensional solids, Rev. Mod. Phys. **90**, 015001 (2018).

[13] S. Nakatsuji, N. Kiyohara, and T. Higo, Large anomalous Hall effect in a non-collinear antiferromagnet at room temperature, Nature (London) **527**, 212 (2015).

[14] A. Sakai, Y. P. Mizuta, A. A. Nugroho, R. Sihombing, T. Koretsune, M.-T. Suzuki, N. Takemori, R. Ishii, D. Nishio-Hamane, R. Arita *et al.*, Giant anomalous Nernst effect and quantum-critical scaling in a ferromagnetic semimetal, Nat. Phys. **14**, 1119 (2018).

[15] E. Liu, Y. Sun, N. Kumar, L. Muechler, A. Sun, L. Jiao, S.-Y. Yang, D. Liu, A. Liang, Q. Xu *et al.*, Giant anomalous Hall

effect in a ferromagnetic kagome-lattice semimetal, Nat. Phys. **14**, 1125 (2018).

[16] D. F. Liu, A. J. Liang, E. K. Liu, Q. N. Xu, Y. W. Li, C. Chen, D. Pei, W. J. Shi, S. K. Mo, P. Dudin *et al.*, Magnetic Weyl semimetal phase in a kagomé crystal, Science **365**, 1282 (2019).

[17] I. Belopolski, K. Manna, D. S. Sanchez, G. Chang, B. Ernst, J. Yin, S. S. Zhang, T. Cochran, N. Shumiya, H. Zheng *et al.*, Discovery of topological Weyl fermion lines and drumhead surface states in a room temperature magnet, Science **365**, 1278 (2019).

[18] Y. Machida, S. Nakatsuji, S. Onoda, T. Tayama, and T. Sakakibara, Time-reversal symmetry breaking and spontaneous Hall effect without magnetic dipole order, Nature (London) **463**, 210 (2010).

[19] X. Wan, A. M. Turner, A. Vishwanath, and S. Y. Savrasov, Topological semimetal and Fermi-arc surface states in the electronic structure of pyrochlore iridates, Phys. Rev. B **83**, 205101 (2011).

[20] P. Goswami, B. Roy, and S. Das Sarma, Competing orders and topology in the global phase diagram of pyrochlore iridates, Phys. Rev. B **95**, 085120 (2017).

[21] K. Ladovrechis, T. Meng, and B. Roy, Competing magnetic orders and multipolar Weyl fermions in 227 pyrochlore iridates, Phys. Rev. B **103**, L241116 (2021).

[22] T. Ohtsuki, Z. Tian, A. Endo, M. Halim, S. Katsumoto, Y. Kohama, K. Kindo, M. Lippmaa, and S. Nakatsuji, Strain-induced spontaneous Hall effect in an epitaxial thin film of a Luttinger semimetal, Proc. Natl. Acad. Sci. USA **116**, 8803 (2019).

[23] T. Kondo, M. Nakayama, R. Chen, J. J. Ishikawa, E. G. Moon, T. Yamamoto, Y. Ota, W. Malaeb, H. Kanai, Y. Nakashima *et al.*, Quadratic Fermi node in a 3D strongly correlated semimetal, Nat. Commun. **6**, 10042 (2015).

[24] B. Cheng, T. Ohtsuki, D. Chaudhuri, S. Nakatsuji, M. Lippmaa, and N. P. Armitage, Dielectric anomalies and interactions in the three-dimensional quadratic band touching Luttinger semimetal $Pr_2Ir_2O_7$, Nat. Commun. **8**, 2097 (2017).

[25] D. Pesin and L. Balents, Mott physics and band topology in materials with strong spin-orbit interaction, Nat. Phys. **6**, 376 (2010).

[26] Z. Tian, Y. Kohama, T. Tomita, H. Ishizuka, T. H. Hsieh, J. J. Ishikawa, K. Kindo, L. Balents, and S. Nakatsuji, Field-induced quantum metal-insulator transition in the pyrochlore iridate $Nd_2Ir_2O_7$, Nat. Phys. **12**, 134 (2016).

[27] S. Nakatsuji, Y. Machida, Y. Maeno, T. Tayama, T. Sakakibara, J. van Duijn, L. Balicas, J. N. Millican, R. T. Macaluso, and J. Y. Chan, Metallic spin-liquid behavior of the geometrically frustrated Kondo lattice $Pr_2Ir_2O_7$, Phys. Rev. Lett. **96**, 087204 (2006).

[28] E.-G. Moon, C. Xu, Y. B. Kim, and L. Balents, Non-Fermi-liquid and topological states with strong spin-orbit coupling, Phys. Rev. Lett. **111**, 206401 (2013).

[29] Y. Tokiwa, J. Ishikawa, S. Nakatsuji, and P. Gegenwart, Quantum criticality in a metallic spin liquid, Nat. Mater. **13**, 356 (2014).

[30] I. F. Herbut and L. Janssen, Topological Mott insulator in three-dimensional systems with quadratic band touching, Phys. Rev. Lett. **113**, 106401 (2014).

[31] S. Tchoumakov and W. Witczak-Krempa, Dielectric and electronic properties of three-dimensional Luttinger semimetals with a quadratic band touching, Phys. Rev. B **100**, 075104 (2019).

[32] I. Boettcher, Optical response of Luttinger semimetals in the normal and superconducting states, Phys. Rev. B **99**, 125146 (2019).

[33] A. Mauri and M. Polini, Dielectric function and plasmons of doped three-dimensional Luttinger semimetals, Phys. Rev. B **100**, 165115 (2019).

[34] J. M. Link and I. F. Herbut, Hydrodynamic transport in the Luttinger-Abrikosov-Beneslavskii non-Fermi liquid, Phys. Rev. B **101**, 125128 (2020).

[35] H. Freire and I. Mandal, Thermoelectric and thermal properties of the weakly disordered non-Fermi liquid phase of Luttinger semimetals, Phys. Lett. A **407**, 127470 (2021).

[36] I. Mandal and H. Freire, Transport in the non-Fermi liquid phase of isotropic Luttinger semimetals, Phys. Rev. B **103**, 195116 (2021).

[37] A. A. Abrikosov and S. D. Beneslavskii, Possible existence of substances intermediate between metals and dielectrics, Zh. Eksp. Teor. Fiz. **59**, 1280 (1970) [JETP **32**, 699 (1971)].

[38] M. Nakayama, T. Kondo, Z. Tian, J. J. Ishikawa, M. Halim, C. Bareille, W. Malaeb, K. Kuroda, T. Tomita, S. Ideta *et al.*, Slater to Mott crossover in the metal to insulator transition of $Nd_2Ir_2O_7$, Phys. Rev. Lett. **117**, 056403 (2016).

[39] K. Wang, B. Xu, C. W. Rischau, N. Bachar, B. Michon, J. Teyssier, Y. Qiu, T. Ohtsuki, B. Cheng, N. P. Armitage *et al.*, Unconventional free charge in the correlated semimetal $Nd_2Ir_2O_7$, Nat. Phys. **16**, 1194 (2020).

[40] K. Tomiyasu, K. Matsuhira, K. Iwasa, M. Watahiki, S. Takagi, M. Wakeshima, Y. Hinatsu, M. Yokoyama, K. Ohoyama, and K. Yamada, Emergence of magnetic long-range order in frustrated pyrochlore $Nd_2Ir_2O_7$ with metal-insulator transition, J. Phys. Soc. Jpn. **81**, 034709 (2012).

[41] H. Guo, K. Matsuhira, I. Kawasaki, M. Wakeshima, Y. Hinatsu, I. Watanabe, and Z.-A. Xu, Magnetic order in the pyrochlore iridate $Nd_2Ir_2O_7$ probed by muon spin relaxation, Phys. Rev. B **88**, 060411(R) (2013).

[42] Y. Xu, Y. Yang, J. Teyssier, T. Ohtsuki, Y. Qiu, S. Nakatsuji, D. van der Marel, N. Perkins, and N. Drichko, Ramification of

complex magnetism in $Nd_2Ir_2O_7$ observed by Raman scattering spectroscopy, arXiv:2302.00579.

[43] T. P. Devereaux and R. Hackl, Inelastic light scattering from correlated electrons, Rev. Mod. Phys. **79**, 175 (2007).

[44] G. Chen and M. Hermele, Magnetic orders and topological phases from *f-d* exchange in pyrochlore iridates, Phys. Rev. B **86**, 235129 (2012).

[45] F. Ishii, Y. P. Mizuta, T. Kato, T. Ozaki, H. Weng, and S. Onoda, First-principles study on cubic pyrochlore iridates $Y_2Ir_2O_7$ and $Pr_2Ir_2O_7$, J. Phys. Soc. Jpn. **84**, 073703 (2015).

[46] H. Shinaoka, Y. Motome, T. Miyake, S. Ishibashi, and P. Werner, First-principles studies of spin-orbital physics in pyrochlore oxides, J. Phys.: Condens. Matter **31**, 323001 (2019).

[47] H. Zhang, K. Haule, and D. Vanderbilt, Metal-insulator transition and topological properties of pyrochlore iridates, Phys. Rev. Lett. **118**, 026404 (2017).

[48] R. Wang, A. Go, and A. J. Millis, Electron interactions, spin-orbit coupling, and intersite correlations in pyrochlore iridates, Phys. Rev. B **95**, 045133 (2017).

[49] Y. Xu, H. Man, N. Tang, T. Ohtsuki, S. Baidya, S. Nakatsuji, D. Vanderbilt, and N. Drichko, Phonon spectrum of $Pr_2Zr_2O_7$ and $Pr_2Ir_2O_7$ as evidence of coupling of the lattice with electronic and magnetic degrees of freedom, Phys. Rev. B **105**, 075137 (2022).

[50] R. Hackl, M. Opel, P. F. Müller, G. Krug, B. Stadlober, R. Nemetschek, H. Berger, and L. Forró, Electronic Raman scattering in CuO_2 superconductors, J. Low Temp. Phys. **105**, 733 (1996).

[51] Exact formula for the fit: $\chi''(\omega) = 0.059 + 0.25\tau\omega/[1 + (\tau\omega)^2]$, with $\tau^{-1} = 41$ meV for 35–45 K averaged spectra.

[52] M. Kavai, J. Friedman, K. Sherman, M. Gong, I. Giannakis, S. Hajinazar, H. Hu, S. E. Grefe, J. Leshen, Q. Yang *et al.*, Inhomogeneous Kondo-lattice in geometrically frustrated $Pr_2Ir_2O_7$, Nat. Commun. **12**, 1377 (2021).

[53] Y. Li, C.-H. Cheung, and G. Xu, Topological Luttinger semimetallic phase accompanied with surface states realized in silicon, Phys. Rev. B **105**, 035136 (2022).

[54] T. Inoshita, M. Hirayama, N. Hamada, H. Hosono, and S. Murakami, Topological semimetal phases manifested in transition metal dichalcogenides intercalated with 3*d* metals, Phys. Rev. B **100**, 121112(R) (2019).

[55] H.-Y. Lu and Q.-H. Wang, Electronic Raman scattering in graphene, Chin. Phys. Lett. **25**, 3746 (2008).

[56] O. Kashuba and V. I. Fal'ko, Signature of electronic excitations in the Raman spectrum of graphene, Phys. Rev. B **80**, 241404(R) (2009).

[57] O. Kashuba and V. I. Fal'ko, Role of electronic excitations in magneto-Raman spectra of graphene, New J. Phys. **14**, 105016 (2012).

[58] E. Riccardi, M.-A. Méasson, M. Cazayous, A. Sacuto, and Y. Gallais, Gate-dependent electronic Raman scattering in graphene, Phys. Rev. Lett. **116**, 066805 (2016).

[59] I. Mandal and H. Freire, Raman response and shear viscosity in the non-Fermi liquid phase of Luttinger semimetals, J. Phys.: Condens. Matter **34**, 275604 (2022).

[60] J. N. Millican, R. T. Macaluso, S. Nakatsuji, Y. Machida, Y. Maeno, and J. Y. Chan, Crystal growth and structure of $R_2Ir_2O_7$ (R = Pr, Eu) using molten KF, Mater. Res. Bull. **42**, 928 (2007).

[61] K. Ueda, J. Fujioka, Y. Takahashi, T. Suzuki, S. Ishiwata, Y. Taguchi, and Y. Tokura, Variation of charge dynamics in the course of metal-insulator transition for pyrochlore-type $Nd_2Ir_2O_7$, Phys. Rev. Lett. **109**, 136402 (2012).

[62] D. E. Newbury and N. W. Ritchie, Performing elemental microanalysis with high accuracy and high precision by scanning electron microscopy/silicon drift detector energy-dispersive X-ray spectrometry (SEM/SDD-EDS), J. Mater. Sci. **50**, 493 (2015).

[63] L. Wang, B. Yu, R. Jing, X. Luo, J. Zeng, J. Li, I. Bialo, M. Bluschke, Y. Tang, J. Freyermuth *et al.*, Doping-dependent phonon anomaly and charge-order phenomena in the $HgBa_2CuO_{4+\delta}$ and $HgBa_2CaCu_2O_{6+\delta}$ superconductors, Phys. Rev. B **101**, 220509(R) (2020).

Correction: Support information in the last sentence in the Acknowledgment section was incomplete and has been fixed.